

CARBIDE AND MATRIX MICROSTRUCTURE EVOLUTION OF HIGH-VANADIUM WEAR-RESISTANCE CAST IRON WITH HIGH-SILICON CONTENT DURING AUSTEMPERING

Wanqing Leng 

School of Materials Science and Engineering, Henan University of Science and Technology, Luoyang 471003, China

Liujie Xu

School of Materials Science and Engineering, Henan University of Science and Technology, Luoyang 471003, China
National Joint Engineering Research Center for Abrasion Control and Molding of Metal Materials, Henan University of Science and Technology, Luoyang 471003, China

Tao Jiang, Xiaodong Wang and Shizhong Wei

National Joint Engineering Research Center for Abrasion Control and Molding of Metal Materials, Henan University of Science and Technology, Luoyang 471003, China

Xinwei Shi

School of Physics and Microelectronics, Zhengzhou University, Zhengzhou 450001, China

Ming Li

State Key Laboratory of Vanadium and Titanium Resources Comprehensive Utilization, Pangang Group Research Institute Co., Ltd, Panzhihua 617000, Sichuan, China

Copyright © 2022 American Foundry Society
<https://doi.org/10.1007/s40962-022-00886-7>

Abstract

The nanobainite microstructure was fabricated on the high-vanadium cast iron with high silicon content, and the measures of casting and austempering were taken. The results showed that the as-cast microstructure is mainly composed of VC, M_7C_3 , Fe_3C , ferrite, and austenite. After austempering, the acicular M_2C -type carbides precipitated from skeletal M_7C_3 -type carbides, causing a decrease in Cr content in M_7C_3 and the morphology change of M_7C_3 , and the molecular formula of M_7C_3 changed from the $(Fe_{0.61}Cr_{0.19}Mo_{0.12}V_{0.06}Mn_{0.02})_7C_3$ to the $(Fe_{0.41}Cr_{0.36}Mo_{0.09}V_{0.11}Mn_{0.03})_7C_3$, and the morphology of M_7C_3

changes from skeletal shape to net shape. There is no apparent change in the morphology and chemical composition of VC. And the transformation of the matrix microstructure from pearlite to a mixed structure of bunched nanobainite and retained austenite happened. It turned out that the thickness of bainite ferrite and the film retained austenite is 50–110 nm and 30–90 nm, respectively.

Keywords: high-vanadium alloy, high-silicon, austempering, nanobainite, carbides

Introduction

The cold roller of high chromium cast iron and high-speed steel refers to the compound roller with the working layer of high chromium cast iron and high-speed steel.¹

Carbides, including M_6C -, M_7C_3 -, M_2C -, and MC -type carbides,² which are usually formed by design can greatly improve the strength, wear-resistance, and roughness of cold rollers.³ Therefore, the rollers with these above carbides are also called the carbide-reinforcement steels. Among so many carbides-reinforcement steels, the high-vanadium high-speed steel takes a position in wear-resistant steels because of high hardness of matrix⁴ and

reinforcing phase of VC carbides. People manufacture high chromium cast iron cold rollers and high-vanadium high-speed steel cold rollers to supply the increasing demand for rollers with high hardness and excellent wear resistance.⁵

Researches on high-vanadium high-speed steel show that there are several main measures to be taken to ensure the wear resistance of it, which include controlling carbide, improving the morphology of carbide, and regulating matrix characteristics. The high hardness and enough toughness help the matrix structure resist micro-cutting and fatigue wear⁶ in the process of wear. High-carbon high-vanadium content in high-vanadium high-speed steel is favorable for the formation of high hardness martensite with high-carbon supersaturation degree and high hardness MC-type carbides. Modification treatment makes the access of spherical or crumb^{7,8} primary vanadium carbide evenly distributed on the matrix, which is good for the wear resistance. The partially coherent relationship between VC boundaries and matrix interface⁹ can delay the initiation of interface cracks, and the well-shaped VC contributes to the passivation of cracks¹⁰ and improves the anti-fatigue performance and life of rolls.¹¹

But less measures can be taken to improve the wear resistance of high-vanadium high-speed steel. The matrix of high-vanadium high-speed steel is mainly composed of martensite and retained austenite attained by the usual heat treatment process of quenching and tempering, so there has to be a trade-off between the impact toughness and the hardness of the matrix. In addition, the morphology and distribution of most carbides⁸ have been determined during solidification process and are difficult to be shaped again. To improve the wear resistance of high-vanadium high-speed steel, it is worthy for an attempt on regulating the matrix.

Nanobainite is a product phase of austempering at low temperature, characterized by a bunch of nanosized bainite ferrite sheets and carbon-rich retained austenite films between or within the sheets.¹² Due to the incomplete transformation of bainite transformation, massive and thin-film retained austenites are kept among the structures. Studies show the high-carbon and high-silicon nanobainitic steels¹³ are excellent in mechanical properties with a hardness of 600–670 HV, a tensile strength of 2500 MPa, and fracture toughness of 30–40 MPam^{1/2}. And the transformation from austenite to martensite and microplasticity behavior¹⁴ of nanobainite microstructure leads to the increment of hardness, thus improving the sliding wear

resistance of alloy.^{15,16} Similar test results of excellent mechanical properties^{17–22} also show that the steel with this structure has a yield strength of 1400 MPa, a tensile strength of 2200 MPa, an elongation of 30%, and a fracture toughness of about 51 MPam^{1/2}.

There are extensive researches on the nanobainitic steel, but rarely focus on the cast iron with so much carbide. We tried in this study to introduce this type of nanobainite into a high-carbon and high-vanadium alloy to get the nanobainitic cast iron with kinds of carbides with high hardness. Without changing carbides inside, the matrix will be capability of both high hardness and higher impact toughness.

In this work, we have made the nanobainitic cast iron and studied the characteristic of the new type of material.

Test Procedure

Testing Materials

According to researches,^{15,17,20,21,23,24} the content of 1.2–3wt% silicon is added into the steel to prevent the precipitation of carbides during austempering process. The chemical composition of the high-vanadium alloy used to prepare nanobainite material is shown as component A in Table 1.

Test of Critical Temperature of Phase Transition

The thermal dilatometer DIL-805 was used to identify the martensite temperature with the cylinder test sample of $\Phi 4 \text{ mm} \times 10 \text{ mm}$, cleaned by sandpaper. The sample was heated to 600 °C at a rate of 10 °C/s and continued to be heated at a lower speed of 1 °C/s to 1000 °C; after holding at 1000 °C for 1 h, it was then cooled down to ambient temperature around 30 °C with the speed of 20 °C/s. The start temperature of martensitic transformation was determined as 149 °C as is shown in Figure 1.

Preparation of Samples

The as-cast sample preparation process was clarified as follows. The raw materials for melting are listed in Table 2. The medium frequency induction melting furnace was adopted for casting, and pre-deoxidation at the later stage of melting was made. To obtain 90% absorptivity of

Table 1. The Chemical Composition of Alloys wt(%)

C	Si	Mn	S	P	Cr	Mo	V	Fe
3.02	2.14	0.70	0.042	0.033	3.85	2.82	9.94	Balance

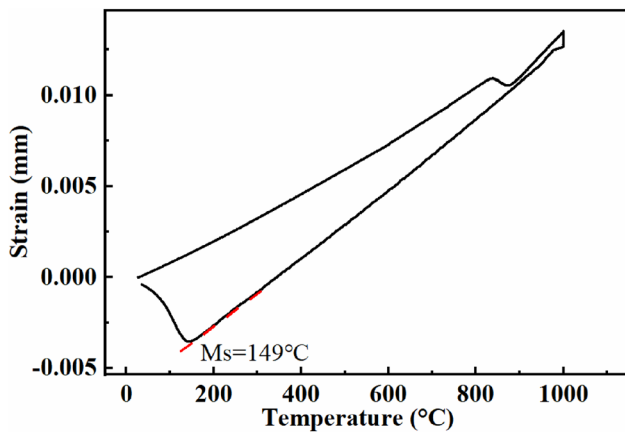


Figure 1. Temperature of initial transformation of martensite on the condition of austenitizing at 1000 °C for 1 h.

Table 2. The Main Charge Materials Used for Melting

Material	Content
Ferrovandium	50–60%V, <2.0%Si
Ferromolybdenum	50–60%Mo
Ferrochrome	50–55%Cr, 4%–10%C
Ferromanganese	> 50%Mn, 1.0–1.7%C
Pig iron	1.25–3.6%Si, 2.5–4%C

vanadium, reaction time at high temperature was minimized after adding ferrovandium to the furnace. Then, the 0.1% pure aluminum was added for final deoxidation and modifying agent of 0.4% SIII (mainly rare earth) was used. The clay sand casting was employed, and the molten liquid was poured from the furnace at 1500 °C and poured into the open sand mold at 1450 °C to get the cuboid likely ingot. Samples in a size of 10*10*10 mm were cut by wire cutting from the same edge of the ingot with the size about 130*100*90 mm and one was for the comparison, the other for heat treatment. The study⁶ showed that the temperature of between 900 and 1100 °C is enough for complete austenitizing, so the austenitizing process was set at 1000 °C for 1 h. As the previous study¹⁴ about nanobainite, austempering above the Ms point is accessible to nanobainite structure. The measured martensite-start temperature was 149 °C according to the phase transformation simulation test taken at 1000 °C for 1 h as depicted in Figure 1, and the one-step austempering was taken at 300 °C. The heat treatment process is shown in Figure 2, and the sample was heated to 1000 °C (+/- 5 °C) at a speed of 10 °C/min and held for 1 h, followed by quenching to the 300 °C (+/- 0.2 °C) melt salt without time interval.

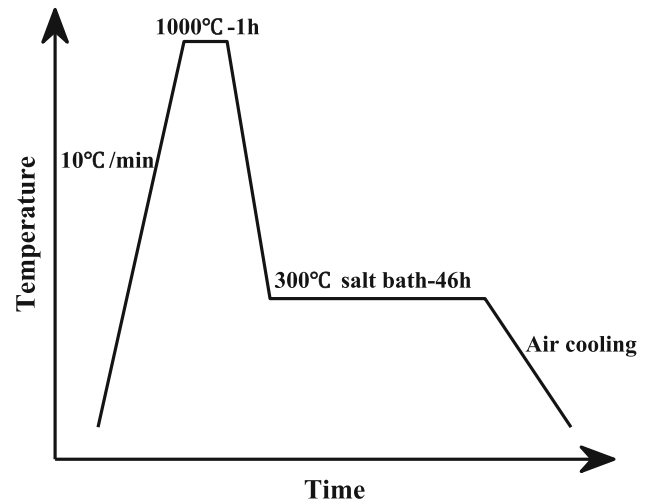


Figure 2. Heat treatment illustration of austempering.

Observation and Analysis of Microstructure

Focus on the microstructures on the center part of samples. The microstructure and sub-microstructure of the as-cast and austempered samples were characterized and analyzed by a JEOL JSM-IT 800 SHL field emission scanning electron microscope (FE-SEM), a scanning electron microscope (SEM), and H-800 type transmission electron microscope (TEM).

The SEM and XRD samples were prepared by wire cutting, milled, and polished according to typical preparation methods for metallographic samples. The SEM samples were deep-etched with 4% nital for several minutes and cleaned with an ultrasonic cleaner for 10 min. To observe the 3D microstructure clear, the sample was even deeper etched in the 4% nital for about thirty minutes. The TEM sample was prepared on a twin jet electron electro-polisher.

The phase constituents and proportions were analyzed by the D8-Advance Bruker (Germany) X-ray diffractometer at 40 kV and 40 mA with the Cu K α radiation, the wavelength $\lambda = 1.54056 \text{ \AA}$. The scanning angle 2θ was set to be from 30° to 90° with the speed of 6°/min, 0.02° for every step. The mass fractions of VC, α -Fe, and λ -Fe are calculated by integrated intensity of (111) profile in austenite, (200) profile in VC, and (110) profile in ferrite, following the equation²⁵:

$$w_j = \frac{I_j}{K_i^j \sum_{i=1}^N \frac{I_i}{K_i^j}} \quad \text{Eqn. 1}$$

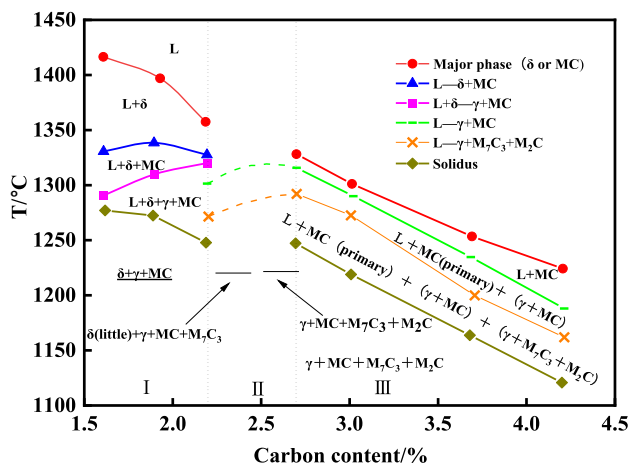


Figure 3. Pseudo-binary phase diagram of (Fe-5Cr-2Mo-9V)-C alloy system.²⁶

Results and Discussion

Phase Transformation of Primary and Eutectic Carbides

According to quasi-binary phase diagrams of (Fe-5Cr-2Mo-9V)-C²⁶ in Figure 3, primary VC precipitates first during the solidification process. With the decrease in temperature and the content of vanadium and carbon, VC and γ -Fe undergo a eutectic reaction. At last, a secondary eutectic reaction will occur with the precipitation of M_7C_3 type or M_2C type carbides.

The XRD pattern shown in Figure 4 revealed that the as-cast structure is mainly composed of α -Fe (ferrite), VC, and the austempered microstructures mainly include α -Fe (ferrite), γ -Fe (retained austenite), VC. The reason for the inconsistency between the phase diagram and the XRD pattern of the as-cast sample may be the undetectable low content of M_7C_3 type carbide. The intensity of the face-centered cubic ferrite diffraction profile indicates an apparent increase in the austempered sample, which matches the nanobainite microstructures composed of austenite and bainite ferrite.

The backscattered electron images of the as-cast and austempered samples are shown in Figure 5, respectively. As can be seen, dark chrysanthemum-like and crumbly vanadium carbides are formed in both the as-cast and austempered microstructures, which is identical to the study results. The heat treatment has little influence on the morphology of VCs.

Seeing that elements of Fe, Cr and Mo are likely to form the carbides except V, the gray and white carbides in the as-cast sample are supposed to be the M_7C_3 or the M_2C type carbide rich in Fe, Cr, and Mo according to the phase diagram. The EDS result in Table 3 shows that the gray carbide of the as-cast sample is M_7C_3 type carbide, while

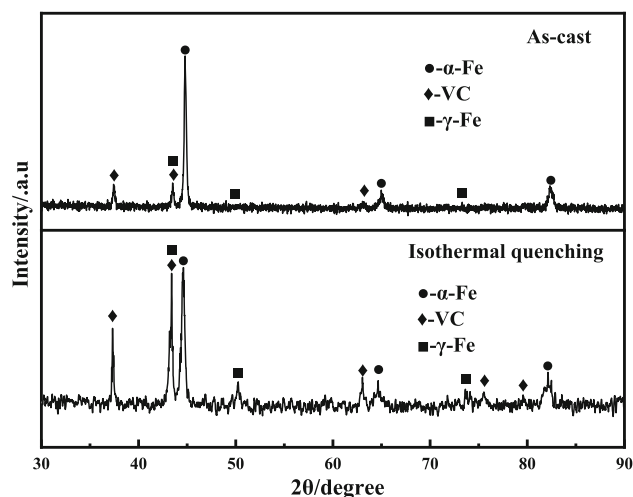


Figure 4. XRD patterns of the as-cast and austempered high-vanadium alloy.

the white and dark carbides of the austempered sample are M_2C and M_7C_3 type carbides. The white acicular carbide in austempered structure suggests that white M_2C carbide grew from M_7C_3 during the long period of the isothermal process.

Effect of Austempering on Primary and Eutectic Carbides

Morphology of Primary and Eutectic Carbides

The microstructure morphology of deeply etched samples is shown in Figure 6, in which Figure 6a, b are images of the as-cast sample, and Figure 6c, d are of the austempered sample. From the comparison of two-dimensional and three-dimensional morphology, the crumbly VC in Figure 5a is nodular in three dimensions, while the VC with chrysanthemum distribution is coral-like. In addition, the horizontal sections of skeleton M_7C_3 are discontinuous and layered with hollow structures. As is shown in Figure 6a, the coral-like VC grows along the direction from the inside toward the grain boundary and is connected with M_7C_3 around the grain boundary.

It can be seen from the above analysis that with the uniform growth resistances in all directions around, it is easy for VC crystal embryos to grow into nodules, as shown in Figure 6a. As the content of carbon and vanadium decreases, and the temperature drops, the carbide grows into dendrite along the solidification direction together with austenite, which is called the eutectic reaction. The growth direction of eutectic carbide is limited by the eutectic solidification process and, finally, grows into dendritic and coralliform. At the end of solidification, Cr and Mo elements are enriched at the grain boundary with the low content of Mo and relatively high content of Cr, so the M_7C_3 -type carbide is formed in the secondary eutectic reaction on boundaries.

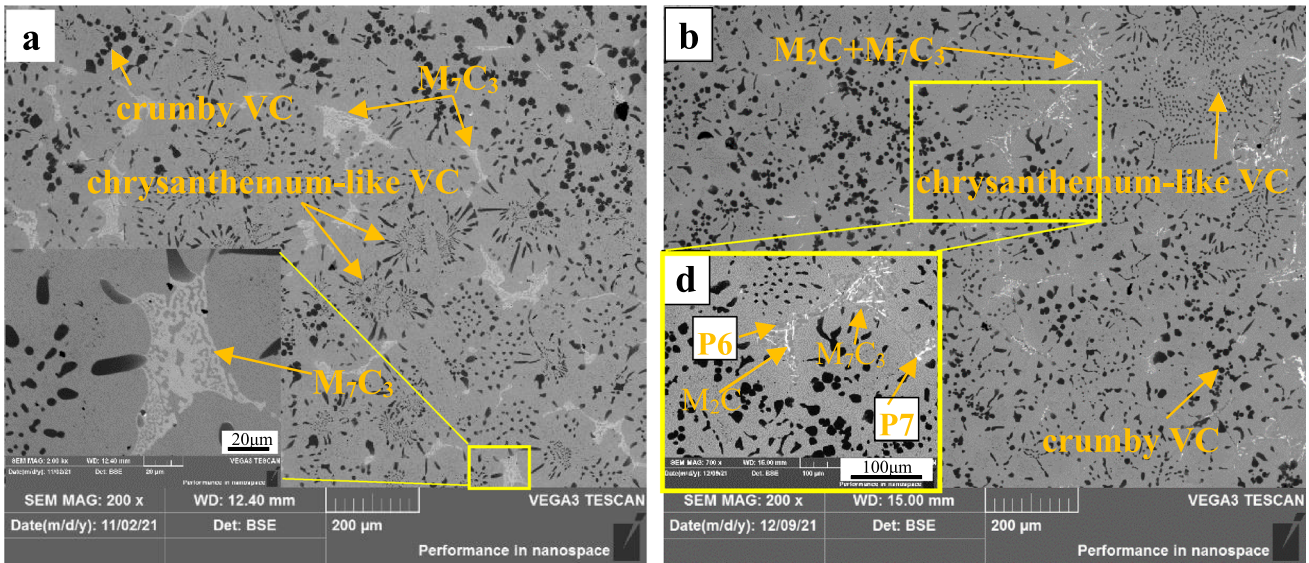


Figure 5. BSE images of high-vanadium alloys: (a) as-cast sample; (b) austempered sample.

Table 3. Chemical Composition of Different Carbides (at%)

Carbide type	C	Mo	V	Cr	Mn	Fe
primary VC (AS)	43.65	1.49	52.61	1.53	0.08	0.64
eutectic VC (AS)	43.84	3.46	47.99	2.92	0.17	1.40
M ₇ C ₃ (AS)	27.63	8.57	4.30	13.10	1.30	41.78
primary VC (IQ)	44.01	1.48	52.84	1.10	0.08	0.08
eutectic VC (IQ)	45.56	4.53	46.02	2.78	0.31	0.39
M ₇ C ₃ (IQ)	37.55	5.89	6.74	22.42	1.67	25.51
M ₂ C (IQ)	37.53	15.24	6.84	14.69	1.54	23.18

AS-as-cast, IQ-austempered

After the austempering, the skeleton M₇C₃ carbide at grain boundary is decomposed into net M₇C₃ carbide and acicular M₂C carbide, and the coral-like VC remains unchanged.

Distribution of Elements in Primary and Eutectic Carbides

From the map scanning result in Figure 7, C and V are mainly distributed in the crumby and chrysanthemum VC, less in M₇C₃-type carbides. The aggregations of Mo and Cr in different carbides are similar with more content in M₇C₃-type carbides, and less in VC.

The scanning patterns of Figures 7 and 8 illustrate that austempering did not change the elements distribution of VCs which are mainly composed of C and V, followed by Mo and Cr. M₂C-type contains higher quality of molybdenum instead of chromium, while the M₇C₃-type carbide consists of chromium, molybdenum, and carbon, with more chromium, and less molybdenum and carbon. In addition to abundant iron content, there is also some chromium evenly distributed in the matrix. And the images of crumby VC and chrysanthemum VC show that a higher concentration of V exists in crumby VC and more quality C, Cr and Mo are formed in chrysanthemum VC.

Compared with the as-cast sample, the distribution of elements V, C and Fe elements in the austempered sample has no obvious change. Most of the carbon and vanadium form VC, and some of them go into the chromium carbide and molybdenum carbide to form carbides. With the decomposition of M₇C₃ carbide into M₂C carbide in the as-cast sample, Cr and Mo elements redistribute in these two carbides. By comparing the distribution features of molybdenum and chromium, the molybdenum and chromium content in microstructure is more uniform among carbides and matrix.

Analysis of the Composition of Primary and Eutectic Carbides

The influence of heat treatment on different carbides and the content of carbide elements is studied further as in Table 3. Compared with chrysanthemum VC (eutectic), crumby VC (primary) contains less carbon, molybdenum, and chromium, but more vanadium, which is caused by the different precipitation order of carbide. Compared with the as-cast sample, the content of elements C and Mo in

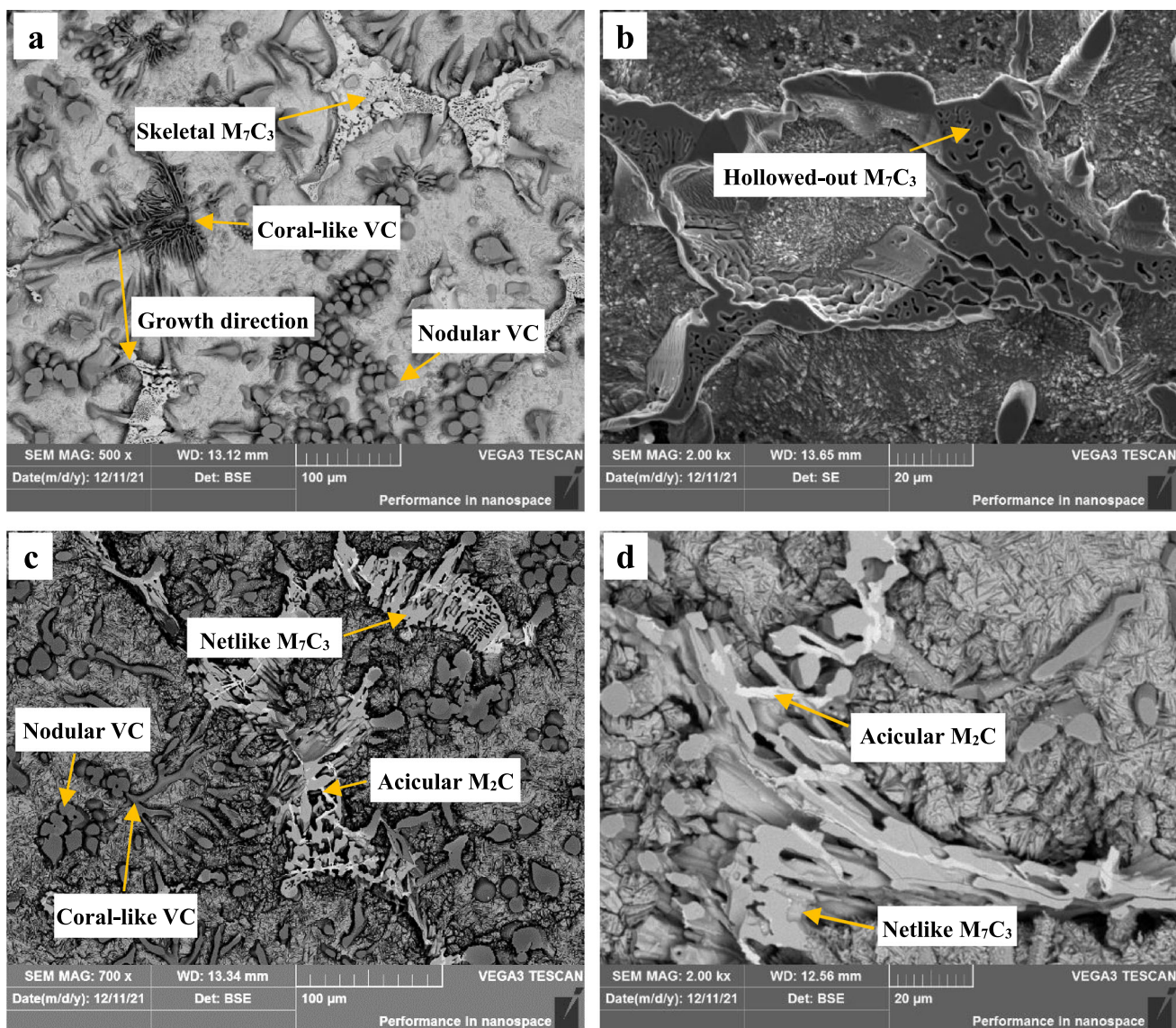


Figure 6. Microstructures of as-cast and austempered alloy: (a), (b) as-cast alloy; (c), (d) austempered alloy.

eutectic VC of the austempered sample increases with decreasing V , which may indicate vanadium's diffusion into the matrix.

The M_2C -type carbide contains C, Mo, V, Cr, Fe and a small amount of Mn, represented as $(Fe_{0.38}Cr_{0.24}Mo_{0.25}V_{0.11}Mn_{0.02})_2C$ calculated by the proportions of elements. M_7C_3 carbide changed from as-cast $(Fe_{0.61}Cr_{0.19}Mo_{0.12}V_{0.06}Mn_{0.02})_7C_3$ into austempered $(Fe_{0.41}Cr_{0.36}Mo_{0.09}V_{0.11}Mn_{0.03})_7C_3$.

Analysis of Submicron VC in Matrix

As displayed in Figures 9 and 11, submicron carbides are found in both the as-cast and heat-treated samples by scanning electron microscope images at high magnification. These carbides are solidification product when the

eutectic reaction happens, which can be identified by the distribution inside the grains and the size quite smaller than the primary carbides.

TEM analysis result in Figure 10 shows that the particle in the austempered sample has FCC structure with a width of about 450 nm. By comparing the accumulation positions of different elements of submicron carbides in heat-treated sample in Figure 11, it is found that the main constituent elements of VC remain unchanged, and the enrichment degree of Cr in these submicron carbides increases.

As shown in Figure 12, measured size distribution of submicron VC in the matrix of samples is plotted. Carbides' sizes of the as-cast and austempered sample are approximately the same, with the diameter ranging from 200 to 700 nm, which means the VCs suffer little effects after the heat treatment. Comparing Figures 9 and 10, VC

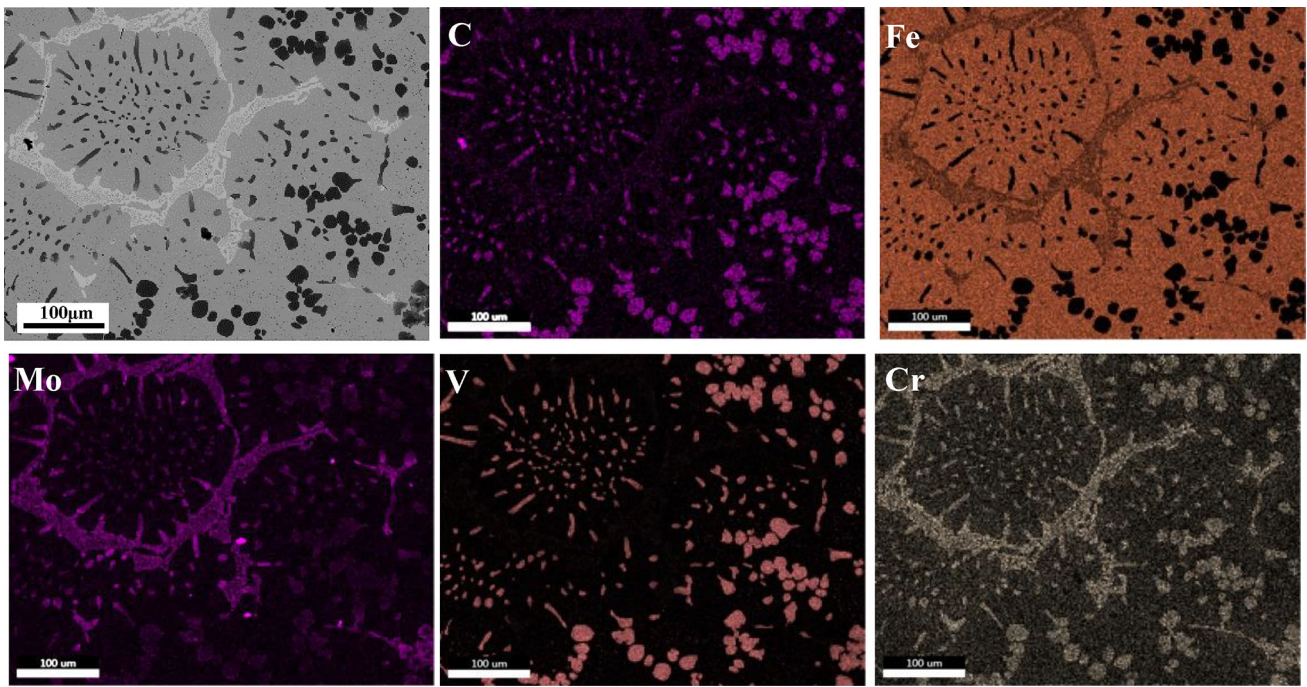


Figure 7. Map scanning result of microstructure of the as-cast high-vanadium alloy.

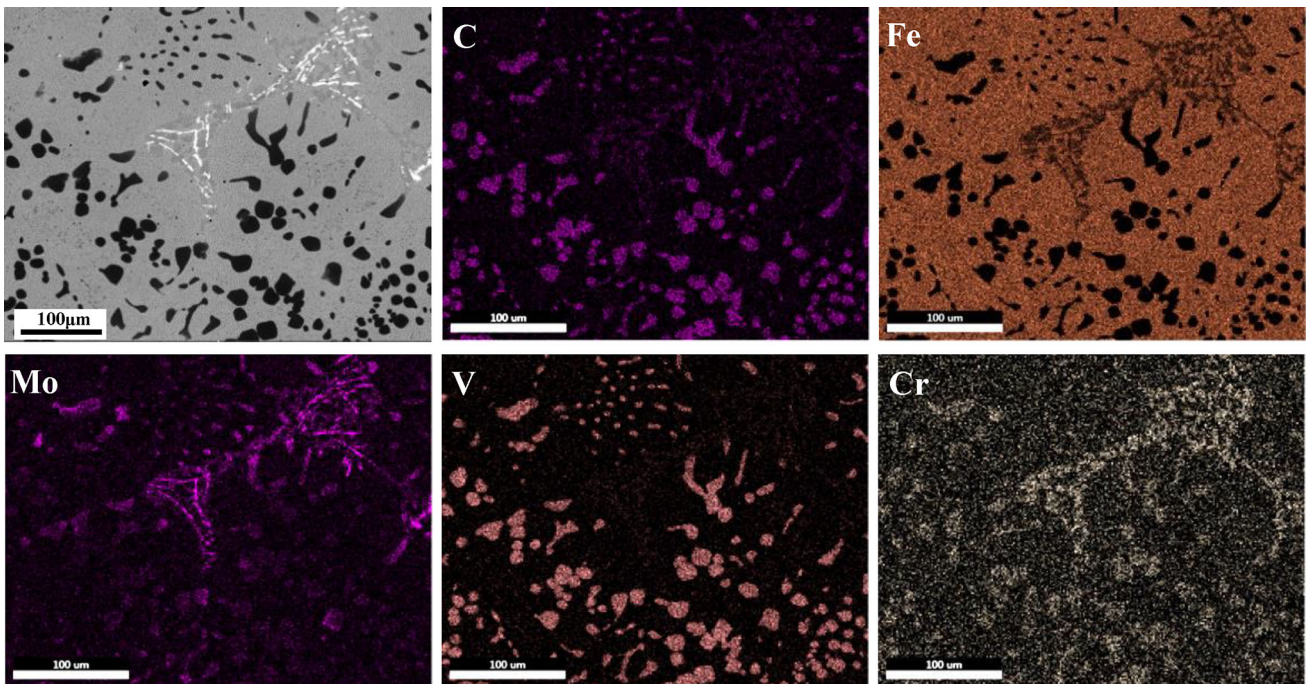


Figure 8. Map scanning result of microstructure of the austempered high-vanadium alloy.

is not distributed by individuals, and quite a few VCs are bonded together.

Based on the above analysis, a conclusion can be made that the submicron VC are about 200 nm to 1 μm. The treatment of austempering has little influence on submicron carbides.

Effect of Austempering on Microstructure of Matrix

According to the high magnification images shown in Figure 13a, b, the as-cast sample is characterized by a fine pearlite with submicron lamellar spacing. After austempering at 300 °C, the matrix structure change into what consists of bunchy nanobainite and massive retained

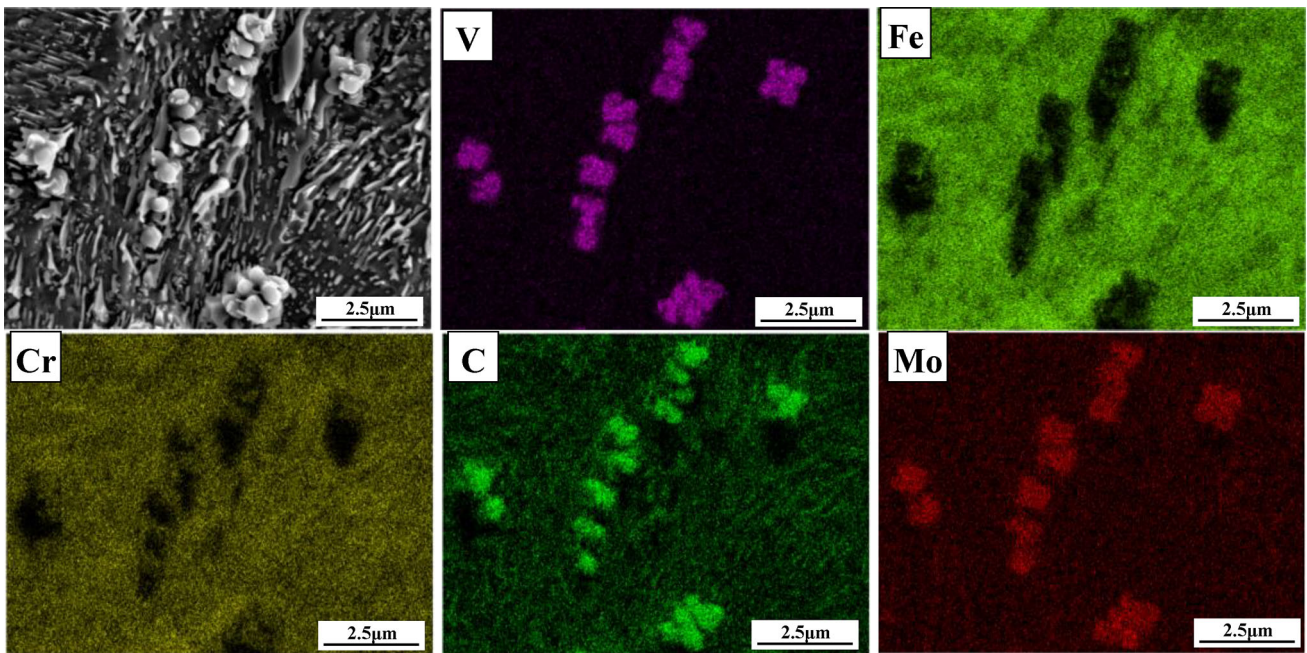


Figure 9. Map scanning analysis result of micron carbides in matrix of as-cast sample.

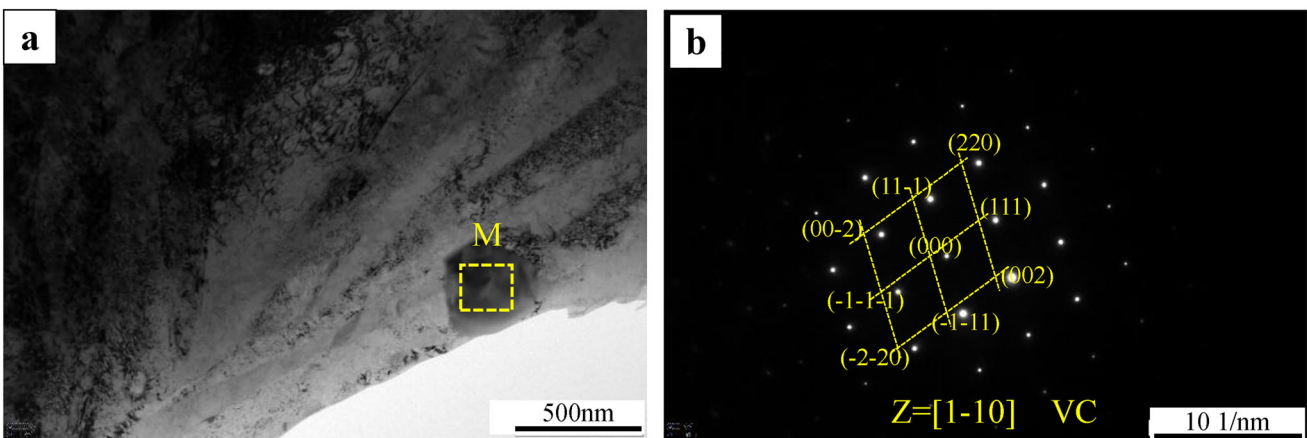


Figure 10. TEM analysis result of submicron carbides in austempered sample (a) TEM image of submicron carbides of austempered sample; (b) selected area diffraction pattern and analysis result of area M in (a).

austenite. From the images and analysis results of Figure 14a–c, the nanobainite package consists of approximately parallel ferrite plates and retained austenite in a thin film. Figure 15 shows the size distribution of bainitic ferrite and film retained austenite in packets according to the linear intercept method,²⁴ which indicates the nanoscale microstructure as other studies. But there are clearly still much amounts of blocky retained austenite, larger than the film austenite, earlier to transform during wear. According to the research of Huang,²⁷ these blocky austenites are more stable under stress to make the steel better in plasticity.

Figure 16a shows the microstructure images obtained by austempering at 300 °C for 46 h. Two kinds of phase transformation products with different features are formed:

bunchy nanobainite and massive retained austenite. And the bunchy bainite in Figure 16b consists of bainite ferrite plate and thin-film austenite with a thickness of several tens of nanometers. There is no carbide precipitation with the bainite ferrite plates and the thin-film austenite. The shape of area E is the same as that of area D, but there is no obvious package inside. Most of the microstructures like the F area are irregular polygonal, and they are massive retained austenite without change. The massive retained austenite has been identified by many studies.^{28,29}

According to the microstructure distribution features in Figure 16a, retained austenites are controlled within the area defined by D and E. The microstructure D, bainite packages, is always longer than that of the surrounding microstructures E among different microstructures D,

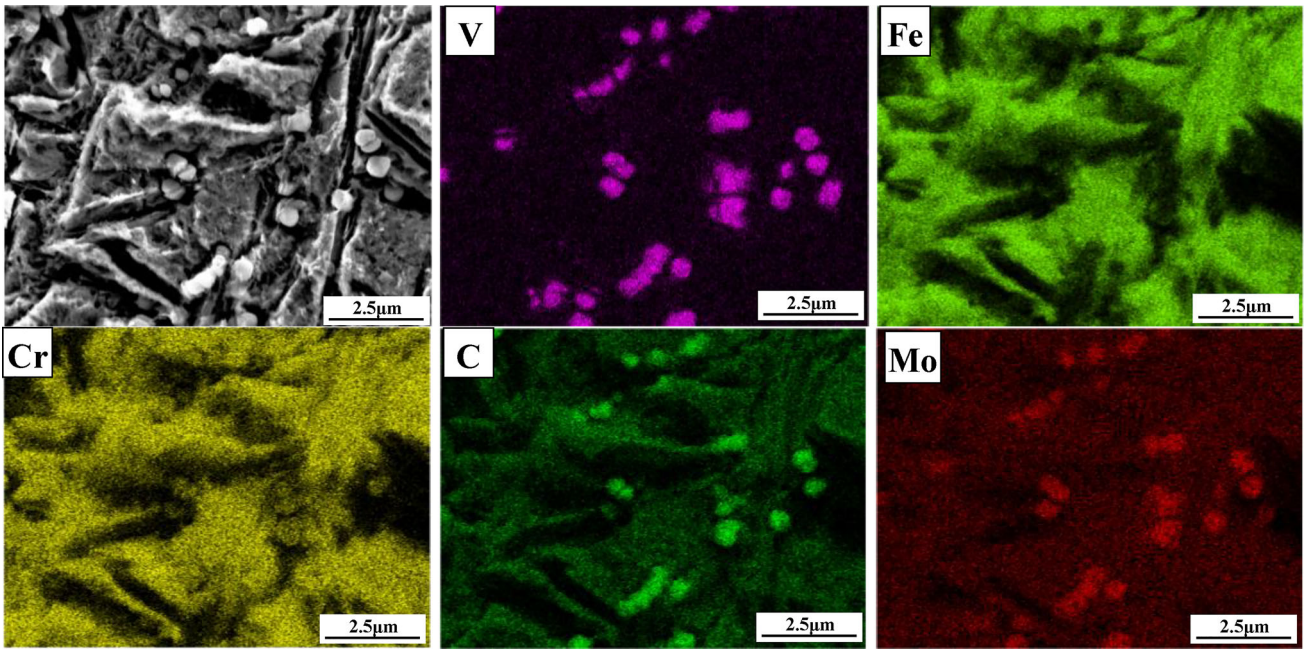


Figure 11. Map scanning analysis result of micron carbides in matrix of austempered sample.

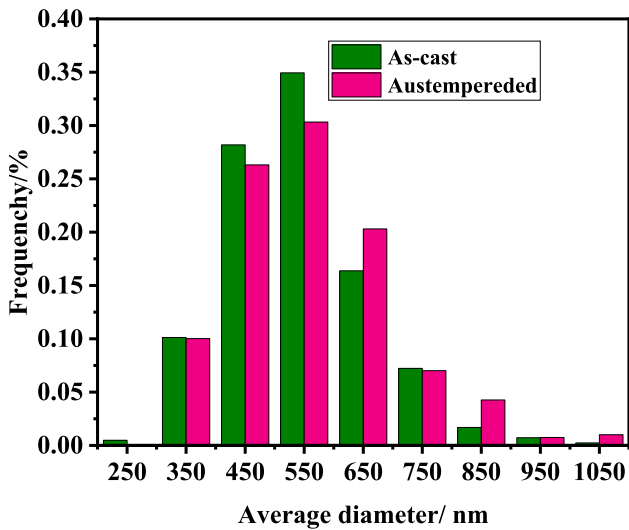


Figure 12. Submicron carbides size distribution of the as-cast and the austempered samples.

which indicates that D nucleates earlier than microstructures E. The microstructure E may be the early stage of D during transformation, which is reasonable. As shown in Figure 16b, the thickness of BF (bainite ferrite) and FA (film austenite) inside G1 and G2 is different, and FA, as well as BF, has a branching structure with finer thickness. Therefore, it can be inferred that bainite microstructure is gradually refined during the isothermal process. Structure I is an early stage in the development of bainite with the development of bainite, and G2 is gradually refined and finally refines into morphological structure similar to G1.

In Figure 16a, bainite with different lengths and thicknesses is mainly related to different nucleation time. The

grain boundary is the preferential position of bainite nucleation, and then, bainite nucleates on the boundary of existed bainite. Some bainite microstructures nucleating earlier penetrated austenite easily without other microstructures getting in the way. The bainite nucleating later has limited space for growth and ends up in a small size. Therefore, the sizes and development degrees of bainite G1, G2, and I are different. As the development of bainite, the thickness of bainite becomes smaller and the retained austenite gets dissolved.

According to the XRD pattern of the isothermally quenched sample, the microstructure of the samples after heat treatment is mainly composed of VC, ferrite, and austenite, the relative contents of which are obtained, and the results are shown in Table 4. From the content of α -Fe and γ -Fe, majority of austenite has transformed, but the microstructure characteristic shows irregularly spacing between the two phases, which may be the origin of cracks when nonuniform transformation takes place.

Conclusion

- (a) High-vanadium wear-resistant alloy with high-silicon content is fabricated by sand casting process. The as-cast microstructure of alloy is mainly composed of VC, M_7C_3 , Fe_3C , ferrite and austenite. Different carbides have different morphology. Primary VC and eutectic VC are spherical and coral-like, while the M_7C_3 carbide and eutectoid submicron VC in the as-cast sample are skeleton and spherical, respectively.

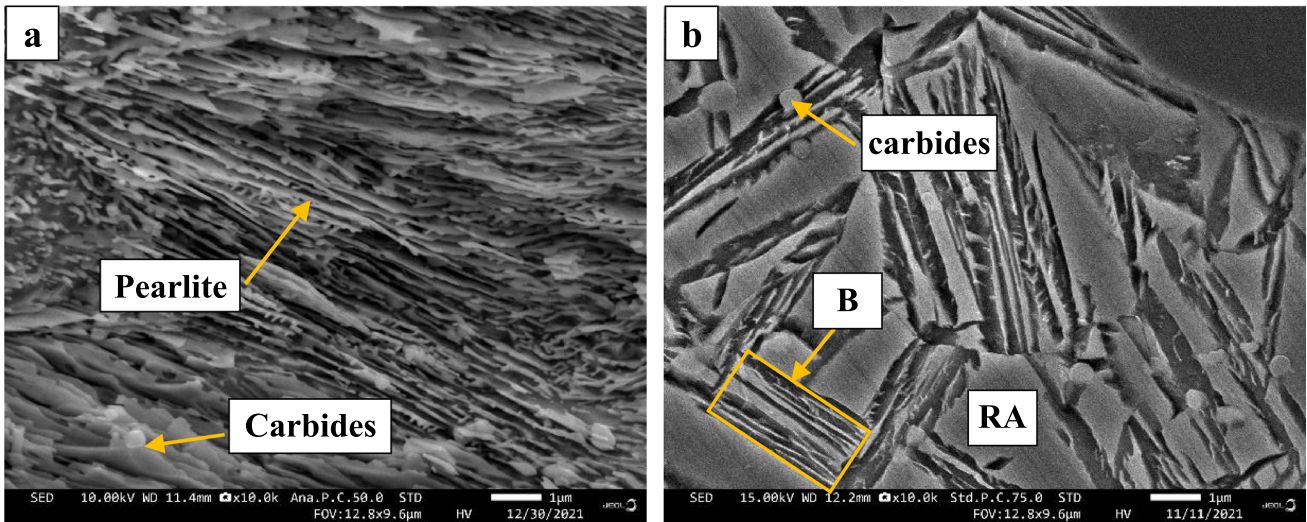


Figure 13. Matrix microstructures: (a) matrix microstructure of the as-cast sample; (b) matrix microstructure of the austempered sample (B-bainite, RA-retained austenite).

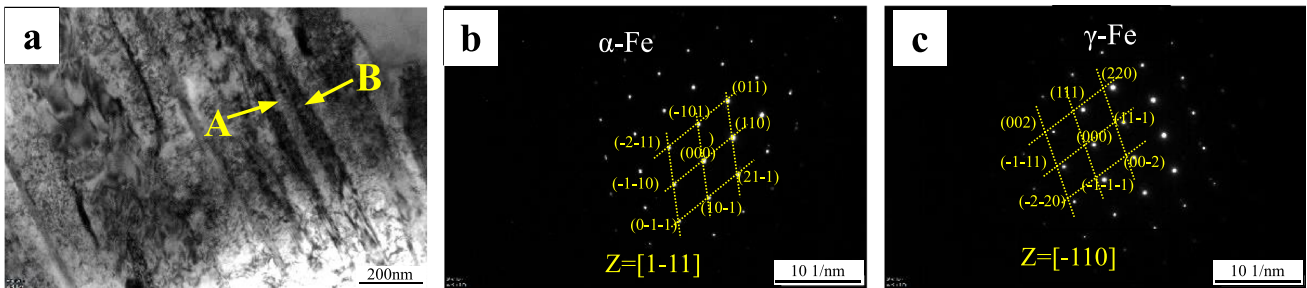


Figure 14. TEM analysis of matrix composed of BF (bainite ferrite) and FA (film austenite) of sample treated by austempering at 300 °C: (a) TEM image of matrix composed of BF and FA; (b), (c) selected area diffraction pattern analysis of area A and B in (a).

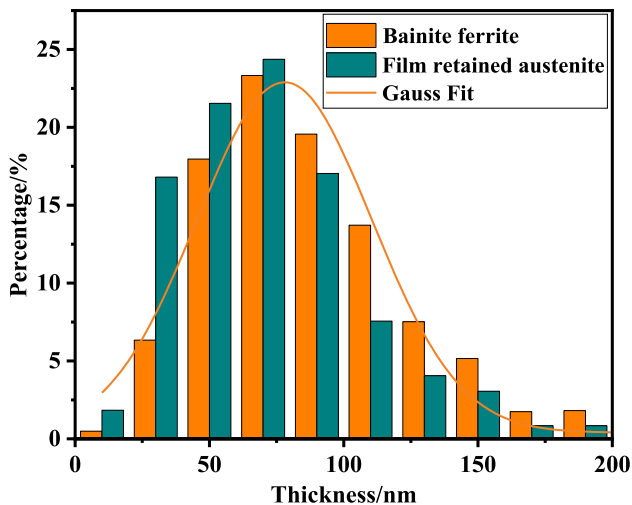


Figure 15. Thickness distribution of the bainite ferrite and film retained austenite in sample after austempering at 300 °C.

- (b) After isothermal quenching, the acicular M_2C -type carbides precipitated from skeletal M_7C_3 -type carbides during isothermal quenching, causing decrease in Cr content in M_7C_3 and morphology change of M_7C_3 . The molecular formula of M_7C_3 changed from as-cast $(Fe_{0.61}Cr_{0.19}Mo_{0.12}V_{0.06}Mn_{0.02})_7C_3$ to isothermal quenching state $(Fe_{0.41}Cr_{0.36}Mo_{0.09}V_{0.11}Mn_{0.03})_7C_3$, and the morphology of M_7C_3 change from skeletal shape to net shape.
- (c) The morphology and chemical composition of VC had no apparent change after isothermal quenching.
- (d) The isothermal quenching caused transformation of matrix microstructure. The matrix changed from pearlite to a mixed structure of bunchy nanobainite and retained austenite. The thickness of bainite ferrite was 50–110 nm, and the thickness of film retained austenite is 30–90 nm.

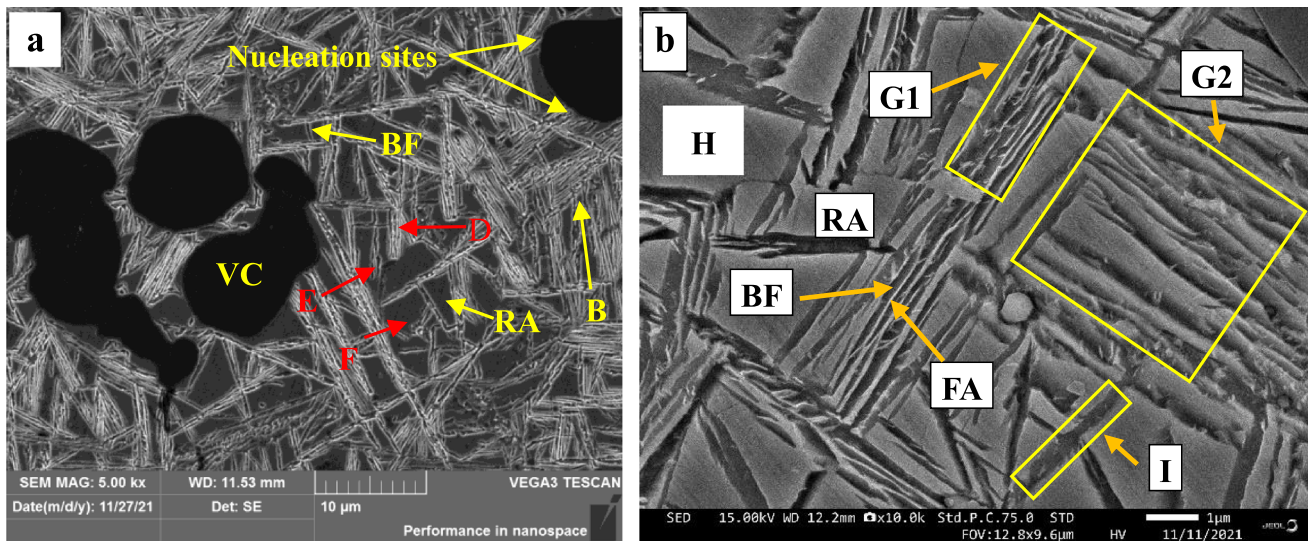


Figure 16. SEM micrographs of microstructures obtained by austempering at 300 °C followed by air cooling (RA-retained austenite, BF-bainite ferrite, FA-film austenite, M-martensite): (a) $\times 5$ k; (b) $\times 10$ k.

Table 4. Relative Content of Phases.

Phase	The as-cast (wt%)	The austempered (wt%)
α -Fe	67.22	44.66
γ -Fe	5.07	23.25
VC	27.70	32.09

Acknowledgments

The authors greatly acknowledge the Plan for National Natural Science Foundation of China (No. 51171060) and Program for Changjiang Scholars and Innovative Research Team in University (IRT1234).

REFERENCES

1. Y.L. Cao, Y.W. Dong, Z.H. Jiang et al., Characteristics of high speed steel/ductile cast iron composite roll manufactured by electroslag remelting cladding. *ISIJ Int.* **61**(7), 2127–2134 (2021). <https://doi.org/10.2355/isijinternational.ISIJINT-2020-594>
2. K. Kamimiyada, S. Ishikawa, H. Miyahara et al., Effect of MC type carbides on wear resistance of high wear resistant cast iron rolls developed for work rolls of hot strip mills. *ISIJ Int.* **61**(10), 2597–2604 (2021). <https://doi.org/10.2355/isijinternational.ISIJINT-2021-127>
3. G.W. Jia, L. Hua, H.J. Mao, The influence of surface layer microstructure evolution of M2 steel cold-ring rolling mandrel roller on fatigue crack initiation. *J. Mater. Process. Technol.* **187–188**, 562–565 (2007). <https://doi.org/10.1016/j.jmatprotec.2006.11.093>
4. V. Vukojevic, S. Jovic, B. Nedeljkovic et al., The effect of vanadium content on microstructure and impact toughness of forged high alloy steel X96CrMo12-1. *Int. J. Metalcast.* **13**(1), 82–88 (2019). <https://doi.org/10.1007/s40962-018-0225-4>
5. F.F. Wang, L.J. Xu, Microstructure and erosion wear characterization of a new cast high-vanadium-chromium alloy (HVCA). *Int. J. Metalcast.* (2022). <https://doi.org/10.1007/s40962-022-00787-9>
6. L.J. Xu, J.D. Xing, S.Z. Wei et al., Study on relative wear resistance and wear stability of high-speed steel with high vanadium content. *Wear* **262**(3–4), 253–261 (2007). <https://doi.org/10.1016/j.wear.2006.05.016>
7. S.Z. Wei, J.H. Zhu, L.J. Xu, Effects of vanadium and carbon on microstructures and abrasive wear resistance of high speed steel. *Tribol. Int.* **39**(7), 641–648 (2006). <https://doi.org/10.1016/j.triboint.2005.04.035>
8. L.J. Xu, H.M. Chen, S.Z. Wei et al., Morphology of in-situ VC ceramics in high speed steel with high vanadium content. *Adv. Mater. Res.* **105–106**, 46–48 (2010). <https://doi.org/10.4028/www.scientific.net/AMR.105-106.46>
9. E. Pereloma, D. Cortie, N. Singh et al., Uncovering the mechanism of dislocation interaction with nanoscale (<4 nm) interphase precipitates in microalloyed ferritic steels. *Mater. Res. Lett.* **8**(9), 341–347 (2020). <https://doi.org/10.1080/21663831.2020.1764121>
10. L.J. Xu, S.Z. Wei, M.R. Han et al., Effect of carbides on wear characterization of high-alloy steels under high-stress rolling-sliding condition. *Tribol. Trans.* **57**(4), 631–636 (2014). <https://doi.org/10.1080/10402004.2014.890265>
11. J. Wang, S.J. Fu, Production of in situ vanadium carbide particulate reinforced iron matrix composite.

- Mater. Sci. Medziagotyra **20**(4), 409–413 (2014). <https://doi.org/10.5755/j01.ms.20.4.6445>
12. S.B. Singh, H.K.D.H. Bhadeshia, Estimation of bainite plate-thickness in low-alloy steels. Mater. Sci. Eng., A **A245**(1), 72–79 (1998). [https://doi.org/10.1016/S0921-5093\(97\)00701-6](https://doi.org/10.1016/S0921-5093(97)00701-6)
 13. H. Amel-Farzad, H.R. Faridi, F. Rajabpour et al., Developing very hard nanostructured bainitic steel. Mater. Sci. Eng., A **559**, 68–73 (2013). <https://doi.org/10.1016/j.msea.2012.08.020>
 14. Z.N. Yang, C.B. Liu, C.Y. Zhang et al., Microplasticity behavior of multiphase high-strength nanobainitic steel based on a modified law of mixtures. Mater. Sci. Eng., A (2021). <https://doi.org/10.1016/j.msea.2021.141848>
 15. V.G. Efremenko, O. Hesse, T. Friedrich et al., Two-body abrasion resistance of high-carbon high-silicon steel: metastable austenite vs nanostructured bainite. Wear **418–419**, 24–35 (2019). <https://doi.org/10.1016/j.wear.2018.11.003>
 16. Z.H. Song, S.H. Zhao, T. Jiang et al., Effect of nanobainite content on the dry sliding wear behavior of an Al-alloyed high carbon steel with nanobainitic microstructure. Materials (Basel) (2019). <https://doi.org/10.3390/ma12101618>
 17. C. Garcia-Mateo, F.G. Caballero, Ultra-high-strength bainitic steels. ISIJ Int. **45**(11), 1736–1740 (2005). <https://doi.org/10.2355/isijinternational.45.1736>
 18. F.C. Zhang, Z.N. Yang, Development of and perspective on high-performance nanostructured bainitic bearing steel. Engineering **5**(2), 319–328 (2019). <https://doi.org/10.1016/j.eng.2018.11.024>
 19. H.J. Liu, J.J. Sun, T. Jiang et al., Improved rolling contact fatigue life for an ultrahigh-carbon steel with nanobainitic microstructure. Scr. Mater. **90–91**, 17–20 (2014). <https://doi.org/10.1016/j.scriptamat.2014.07.006>
 20. O. Rios-Diez, R. Aristizabal-Sierra, C. Serna-Giraldo et al., Wear behavior of nanostructured carbo-austempered cast steels under rolling-sliding conditions. J. Mater. Res. Technol. **11**, 1343–1355 (2021). <https://doi.org/10.1016/j.jmrt.2021.01.094>
 21. P. Kirbis, I. Anzel, R. Rudolf et al., Novel approach of nanostructured bainitic steels' production with improved toughness and strength. Materials (Basel) (2020). <https://doi.org/10.3390/ma13051220>
 22. Y.Z. Du, X.L. Wang, D.Y. Zhang et al., A superior strength and sliding-wear resistance combination of ductile iron with nanobainitic matrix. J. Mater. Res. Technol. **11**, 1175–1183 (2021). <https://doi.org/10.1016/j.jmrt.2021.01.104>
 23. C. Garcia-Mateo, F.G. Caballero, T. Sourmail et al., Tensile behaviour of a nanocrystalline bainitic steel containing 3wt% silicon. Mater. Sci. Eng., A **549**, 185–192 (2012). <https://doi.org/10.1016/j.msea.2012.04.031>
 24. J. Zhao, K. Guo, Y.M. He et al., Extremely high strength achievement in medium-C nanobainite steel. Scr. Mater. **152**, 20–23 (2018). <https://doi.org/10.1016/j.scriptamat.2018.04.005>
 25. J.H. Huang, Z. Li, *X-ray Diffraction of Polycrystalline Materials: Experimental principles, Methods and Applications*, 1st edn. (Metallurgical Industry Press, 2012), p.98
 26. T. Peng, F. Ni, S.Z. Wei et al., Solidification process and phases of V9 HSS with different carbon content. Zhuzao/Foundry **55**(5), 499–504 (2006)
 27. C.C. Huang, M.Q. Zou, L. Qi, Effect of isothermal and pre-transformation temperatures on microstructure and properties of ultrafine bainitic steels. J. Mater. Res. Technol. **12**(2021), 1080–1090 (2021). <https://doi.org/10.1016/j.jmrt.2021.03.038>
 28. W. Gong, Y. Tomota, S. Harjo et al., Effect of prior martensite on bainite transformation in nanobainite steel. Acta Mater. **85**, 243–249 (2015). <https://doi.org/10.1016/j.actamat.2014.11.029>
 29. Y.H. Wang, Z.N. Yang, F.C. Zhang et al., Microstructures and properties of a novel carburizing nanobainitic bearing steel. Mater. Sci. Eng., A (2020). <https://doi.org/10.1016/j.msea.2020.139086>

Publisher's Note Springer Nature remains neutral with regard to jurisdictional claims in published maps and institutional affiliations.

Springer Nature or its licensor (e.g. a society or other partner) holds exclusive rights to this article under a publishing agreement with the author(s) or other rightsholder(s); author self-archiving of the accepted manuscript version of this article is solely governed by the terms of such publishing agreement and applicable law.